Adsorption of Rhodamine B dye from polluted water by *Tinospora cordifolia* modified biochar: Thermodynamic, Kinetic, Adsorption isotherm and Regeneration study

Anjna Kumari, Anita Rani, Ajay Sharma
Department of Chemistry, School of Basic and Applied Sciences, IEC University, Baddi (174103), H.P., India

***Abstract*—Toxic dyes like Rhodamine B must be removed since they contaminate soil and water streams. The potential of *Tinospora cordifolia* stems as an effective bio-adsorbent is investigated in this thorough study, which also compares the adsorption capacity of Rhodamine B dye using a variety of carbon-based adsorbents. This article comprises synthesis of biochar (TSC) from *Tinospora cordifolia* stems, and nanocomposite (TSC/LaCF) by combining biochar with intermixing of Lanthanum nitrate ($La(NO_3).6H_2O$), ferric nitrate ($Fe(NO_3).6H_2O$) and cobalt nitrate ($CoNO_3).6H_2O$ i.e. (LaCF) which was then used as an adsorbent to remove Rhodamine B from polluted water. With 8.6 nm of pore diameter and 54.41 m^2/g of surface area (BET), the resultant biochar was considered as mesoporous having magnetization value of 0.247 emu/g. The SEM study revealed the creation of pores with rough surface texture. Numerous factors, including solution pH, adsorbent dosage, initial dye concentration, contact time, and solution temperature, were used to test and optimize the adsorption experiments. Rhodamine B could be removed with a maximum capacity of 90 % to 38 %. The thermodynamics analysis verified that the adsorption processes were exothermic ($\Delta H° = -12.745$ kJ/mol) and spontaneous ($\Delta S° = -61.784$ kJ/mol).**

***Keywords*—Thermodynamic study; Adsorption; Kinetic study; Porous biochar Polluted water treatment.**

I. INTRODUCTION

Biochar-supported nano-polymers represent an innovative class of hybrid materials that combine the structural advantages of biochar with the functional versatility of nanoscale polymer systems [1-2]. Biochar, a carbon-rich material produced from biomass, provides a porous, stable, and environmentally friendly support that enhances the dispersion and stability of nano-polymeric components [3]. When nanoscale polymers such as stimuli-responsive polymers, conductive polymers, or adsorptive polymeric nanostructures are anchored onto biochar surfaces, the resulting composite exhibits improved mechanical strength, tailored surface chemistry, and enhanced interaction with target compounds [4]. These synergistic features make biochar-supported nano-polymers highly effective for applications such as pollutant adsorption, controlled release systems, catalysis, and environmental remediation. Their sustainability, tunability, and multifunctional behavior position them as promising materials for next-generation environmental and industrial technologies [5].

Activated biochar-supported nano-hetero assemblies are emerging as a highly efficient class of materials designed for environmental purification and resource recovery [6-8]. Activated biochar, derived from biomass through thermal or chemical activation, offers a large surface area, rich porosity, and diverse functional groups that make it an excellent platform for anchoring various nanomaterials. When combined with heterostructured nanoparticles—such as metal oxides, sulfides, carbon nanostructures, or catalytic composites—the resulting hybrid assembly's exhibit enhanced adsorption capacity, improved catalytic activity, and strong structural stability [9-10]. These synergistic systems overcome limitations of individual components, such as nanoparticle aggregation or limited active sites, by creating a multifunctional interface that promotes rapid and selective interactions with contaminants. Because of their sustainability, tunability, and high performance, activated biochar-supported nano-hetero assemblies are gaining significant attention in

fields such as water treatment, soil remediation, energy storage, and environmental catalysis [11-14]. Activated biochar-supported nano-hetero assemblies represent a promising next-generation strategy for the remediation of persistent pollutants in contaminated water systems [15-17]. Biochar, produced from biomass through controlled pyrolysis, offers a highly porous structure, abundant surface functional groups, and excellent chemical stability, making it an ideal support material for nanomaterials. When combined with functional nanoparticles such as metal oxides, carbon-based nanostructures, or catalytic hetero-junctions biochar forms a hybrid platform that enhances adsorption, catalytic degradation, and redox reactions [18-22]. These nano-hetero assemblies leverage synergistic interactions between biochar and the immobilized nanoparticles to accelerate pollutant breakdown, reduce nanoparticle aggregation, and minimize environmental release. As a result, they can effectively remove a wide range of persistent contaminants, including heavy metals, dyes, pharmaceuticals, and emerging organic pollutants [23-25]. Owing to their high efficiency, low cost, and environmental compatibility, activated biochar-based nano-hetero assemblies are increasingly gaining attention as sustainable materials for advanced water purification technologies.

The present manuscript provides a deep insight about the synthesis of Lanthanum-Cobalt ferrites doped nanocomposite (TSC/LaCF) derived from *Tinospora cordifolia* (TSC) stem and , metal nanocomposite procured by the intermixing of Lanthanum nitrate ($La(NO_3).6H_2O$), ferric nitrate ($Fe(NO_3).6H_2O$) and cobalt nitrate ($CoNO_3).6H_2O$ i.e. (LaCF).

Different characterization techniques have been used to observe the nature and composition of the TSC and (TSC/LaCF). The adsorption capacity of (TSC/LaCF) nanocomposite has been verified by studying the thermodynamic and kinetic parameters while removing Rhodamine B dye (pollutant) from the waste water sample.

II. MATERIAL AND METHOD

All the chemicals utilized for this study were of the analytical grades. Rhodamine B dye with molecular weight 319.85 g/mol, with molecular formula of ($C_{16}H_{18}ClN_3S$), was attained from Merck chemicals India, with a standard grade. Chemicals, namely ($La(NO_3).6H_2O$), ($Fe(NO_3).6H_2O$), ($CoNO_3).6H_2O$, HCl, H_2SO_4 and NaOH were procured from Sigma - Aldrich, India. 1000 milliliters of deionized water was diluted with one gram of Rhodamine B dye to get stock solution of 1000 mg L^{-1}.

Prepration of Bio-sorbent from *Tinospora cordifolia* stem:
The stems of *Tinospora cordifolia* were collected from Bilaspur (H.P.), India, and double-distilled water was used to remove any adhering impurities on the sample. The stems were then dried in sunlight for several days. After drying, the material was cleaned, chopped and crushed to get a powder with uniform particle size. The resulting powdered sample was stored in an air tight vial for further analysis.

Preparation of biochar (TSC):
For two and a half hours, the material was pyrolysed at 700 °C in a furnace with temperature increases of 50 °C every 20 minutes. It was allowed to cool overnight after pyrolysis. The biochar was chemically activated by submerging it in solutions of 5% sodium hydroxide (NaOH) and 6% sodium hypochlorite (NaClO). After that, the mixture was heated in a microwave for 30 minutes at 50–60 °C. After that, the activated biochar was filtered and repeatedly rinsed with double-distilled water until the pH was 7, or neutral. The treated biochar (TBC) was then kept for later use after being oven-dried for a whole night at 60 °C.

Synthesis of lanthanum ferrite ($LaFe_2O_3$):
The sol-gel method was used to synthesize the lanthanum ferrites. Lanthanum ferrites ($LaFe_2O_3$) were prepared by adding 0.06M of ferric nitrate ($Fe(NO_3).6H_2O$) and 0.06M of lanthanum nitrate ($La(NO_3).6H2O$) to 30ml of distilled water. To maintain the pH of the aforesaid solution, two to three drops of citric acid ($C_6H_70_8$) were additionally added. A magnetic stirrer was used to heat the mixture to 80°C for ninety minutes straight. The resulting yellowish brown gel was heated, dried for two hours in an oven, and then stored at room temperature.

Preparation of Cobalt ferrites ($CoFe_2O_3$):
The co-precipitation process was used to derive the cobalt ferrite. Using this procedure, the solid was obtained by precipitating two or more soluble

chemicals from a solution. Cobalt nitrate ($CoNo_3$).$6H_2O$ (0.2M) and ferric nitrate ($FeNO_3$.$9H_2O$ (0.6M)) were dissolved in 30ml of distilled water and stirred continuously for 45 minutes at a temperature of 50–60°C to create the cobalt ferrite. To create the metal oxides, a dropwise addition of 0.2M NaOH, or sodium hydroxide, was made to the mixture. The solution was agitated for an hour at 80°C after adding sodium hydroxide once more.

Synthesis of Lanthanum-Cobalt ferrites (LaCF):
Lanthanum ferrite ($LaFe_2O_3$) was dissolved in 45 millilitres of distilled water in a 2:1 ratio in order to prepare lanthanum cobalt ferrites (LaCF). The aforementioned solution was then mixed with cobalt ferrite ($CoFe_2O_3$) and heated to 80°C for 90 minutes while being continuously stirred. They produced brownish precipitates. The precipitates were then cleaned with distilled water, dried in an oven for an hour, and left at room temperature.

Synthesis of biochar encapsulated Lanthanum-Cobalt ferrites Nanocomposite (TSC/LaCF):
To fabricate nanocomposites of lanthanum–cobalt ferrites (LaCF) with biochar (TSC), 3–4 g of activated biochar were incorporated into 50 mL of distilled water. The resultant mixture was then progressively disseminated and agitated on a magnetic stirrer for 90 minutes at room temperature. Next, the obtained lanthanum–cobalt ferrite precipitates were added to the mixture mentioned above. The final solution was refluxed in 50 millilitres of water at 80 to 90 degrees Celsius for four hours. Following completion, the mixture was left to cool before the precipitates (TSC/LaCF) were filtered and dried for an hour in an oven.

Characterization Techniques:
In order to compare various functional groups found in biochar (TSC), metal composite (LaCF), and biochar-based metal nanocomposite (TSC/LaCF), the optical properties of the synthesised nanocomposite (TSC/LaCF) were first examined using an FTIR (PerkinElmer® SpectrumTM 400 FT-IR/NIR spectrometer). X-ray diffraction (XRD) examination was used to assess porosity and crystallinity (X'Pert Pro XRD models). Scanning electron microscopy (SEM, Hitachi SU 8010 Series) was used to analyse surface morphology of obtained products. Furthermore, BET (Quantachrome Autosorb-iQ-MP/XR) was used to quantify the specific surface area and poresize distribution within the nanoparticles; and TGA (RT-2400°C) enables the study of kinetics of chemical reactions, such as evaporation, decomposition, and stability, by examining changes in mass over time or temperature. The pore-size distribution curve was created using the Barett-Joyner-Halenda (BJH) method.

Batch adsorption analysis:
To optimize different factors in the adsorption process, batch adsorption analysis was used. By placing the TSC and TSC/LaCF in a hot air oven at 120º C for two hours, the moisture content was eliminated [26-27]. Rhodamine B dye concentrations ranging from 50 mg/L to 250 mg/L at 303k were combined with the necessary amount of TSC and TSC/LaCF adsorbents in an orbital shaker. A UV spectrophotometer was used to measure the amount of dye that remained after the excess solution was filtered using Whatman filter paper. To ensure the consistent results, the adsorption process was carried out up to three times. The experiment's efficiency (η) and equilibrium adsorption capacity (q_e) and were determined using the following formulas:
(Equation 1 and 2):

$$\eta = (C_o - C_e \times 100)/100 \quad \text{..... Equation (1)}$$

$$q_e = (C_o - C_e \times V)/m \quad \text{..... Equation (2)}$$

Where C_0 and C_e represent the initial and final concentrations of the Rhodamine B dye (mg/L), while, q_e denotes the equilibrium adsorption capacity (mg/g^{-1}).

III. RESULTS AND DISCUSSION

FTIR Study:
FTIR spectra of all three prepared moieties have been shown in (Figure 1). The broad peaks between the region 3500-3227 cm^{-1} indicate presence of hydroxyl group [28]. The peak position between 1700-1300 among all three spectra confirms the C-C stretching vibrations while small peaks at 1040 and 1013 cm^{-1} (Figure 1(a) and (c)) indicate the vibrations due to C-O stretching [29]. Presence of all these bands confirms the existence of different terpenoids, phenolic and carboxylic moiety in

organic as well as in synthesized nanocomposite. Moreover, appearance of different small peaks in the region 800-400 cm^{-1} in (Figure 1 (b) and (c)) give evidence for incorporation of metal nanocomposite (LaCF) into the core of organic moiety (TSC) to form biochar based nanocomposite (TSC/LaCF).

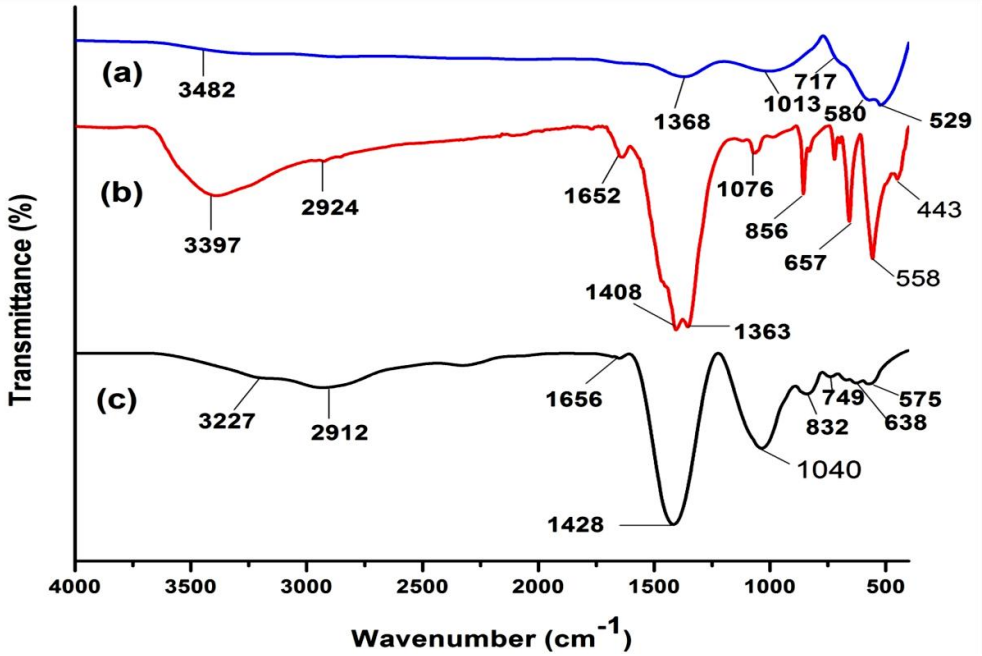

Figure 1: FTIR analysis of (a) TSC (b) LaCF (c) TSC/LaCF nanocomposite

XRD analysis:

(Figure 2) describe the nature of the synthesized nanocomposite and biochar on the basis of crystallinity. (Figure 2 (a)) give evidence about the amorphous behaviour of the biochar (TSC) as not a considerable sharpe peaks are found in maximum region of spectra, while crystallinity appears in (Figure 2 (b) and (c)) in the form of various sharp peaks at different 2 theta value when compared with biochar alone (Figure 2 (a)). These sharp peaks in TSC/LaCF (Figure 2 (c)) signify the proper arrangement of biochar particles after introduction of LaCF. Similarly different peak positions in TSC/LaCF in comparison to TSC and LaCF adds to the confirmation about combination of two moieties and successful synthesis of desired product [30-31].

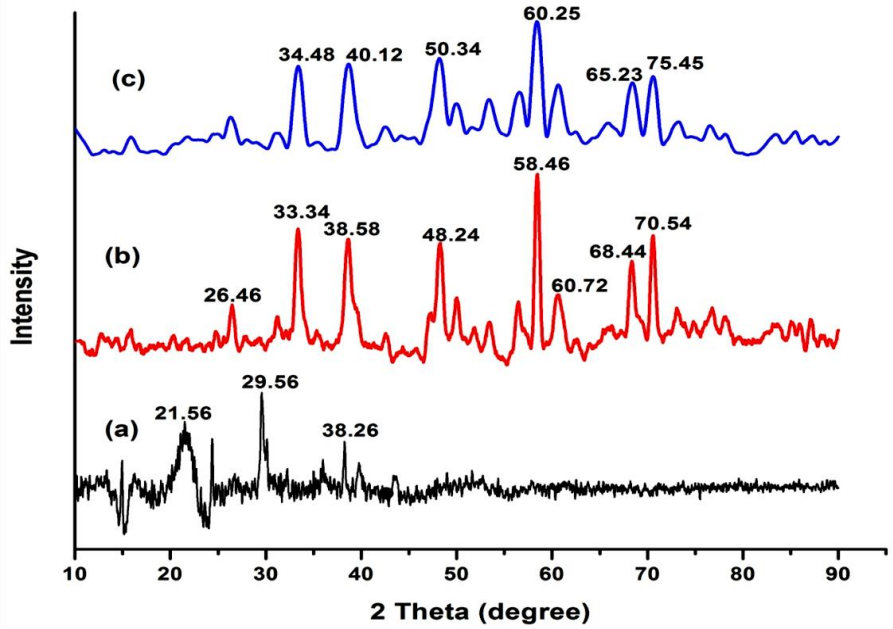

Figure 2: XRD analysis of (a) TSC (b) LaCF (c) TSC/LaCF nanocomposite

FESEM analysis:

Porosity is considered as an essential condition for a substance to be act as good adsorbent. The amorphous or crystalline nature of the synthesized nanocomposite has been validated by XRD spectra. Furthermore, FESEM analysis was done to observe the morphological features of the prepared moieties. (Figure 3 (a-d)) display the porous and homogenous surface of biochar and corresponding nanocomposite. Porosity can be easily found in both the compositions in the form of small voids, which might be arise due to volatilization of different chemicals during the process of carbonization [32-33]. TSC possess tiny rod shaped structure with small voids in between (Figure (a-b)) while TSC/LaCF represent modified homogenous behaviour with spherical features which get implanted among the porous voids of biochar (TSC) (Figure c-d).

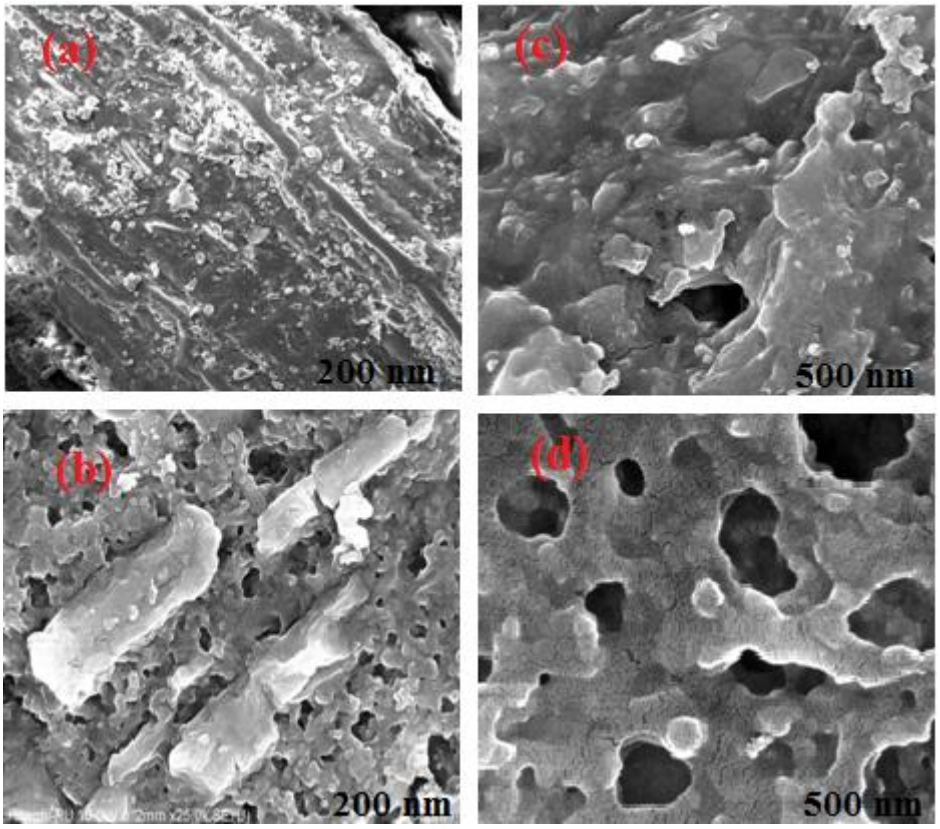

Figure 3: FESEM images of (a and b) TSC and (c and d) TSC/LaCF at different magnifications

VSM analysis:

Using a vibrating sample magnetometer (VSM) with a maximum applied field of 20 kOe at room temperature, the magnetic characteristics of TSC/LaCF was assessed. The prepared sample's magnetic characteristics were verified by the hysteresis loop measured by VSM. The prepared sample's superparamagnetic nature is demonstrated by the hysteresis loop passing across the Cartesian axis in (Figure 4). The substance was identified as soft magnetic material since it had zero coercivity and retentivity [34-35].TSC/LaCF was found to have saturation magnetization values of 0.247 emu/g.

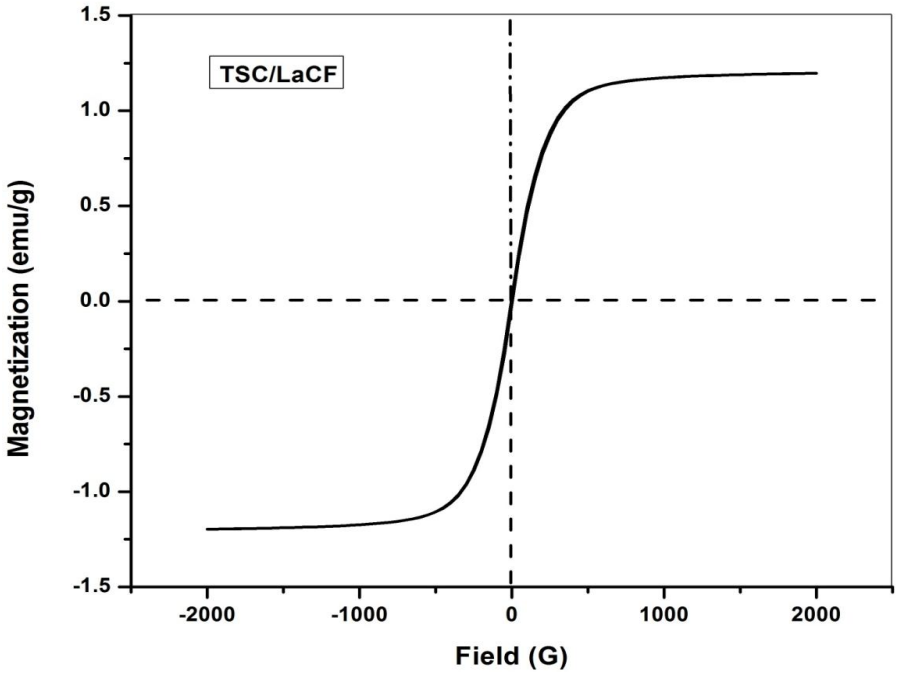

Figure 4: VSM analysis of TSC/LaCF

BET analysis:

The sorption of pollutants in a water system depends on a material's porosity. The three categories of pore size are microporous (less than 2 nm), mesoporous (between 2 and 50 nm), and macroporous (more than 50 nm) [36]. The pore size distribution of TSC/LaCF was ascertained using the Barrett–Joyner–Halenda (BJH) model, which uses the desorption branch of the nitrogen isotherm. The diameter of the highest peaks for the TSC/LaCF nano-structure was measured at 8.6 nm with surface area of 54.41 m^2/g (Figure 5). The increased adsorption absorption of Rhodamine B dye from the water system can be attributed to the constructed nano-hybrid structure, which was discovered in the region of mesoporous nature [37].

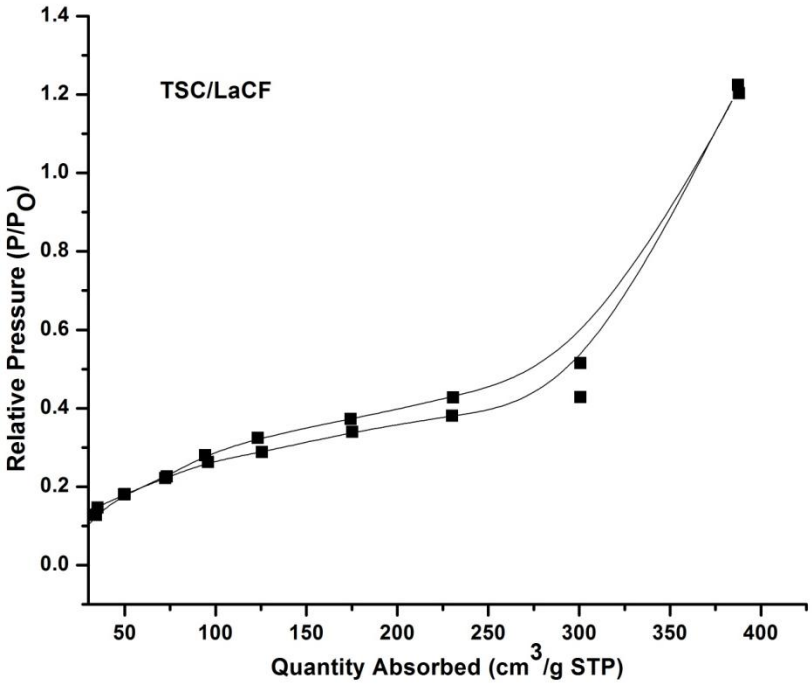

Figure 5: BET adsorption isotherm of TSC/LaCF

TGA Analysis:

The weight loss percentage in relation to temperature was represented by the TGA curve in (Figure 6). Weight decreased as the temperature increased because of several changes brought on by the temperature shift. (Figure 6) suggested that there was 8% drop in weight up to 150^{0}C, indicating that the sample had lost moisture. An additional 50% weight loss was noted when the temperature was increased to 212^{0}C. The breakdown of the organic substance (TSC) in the sample or the disruption of the O-C bond was the causes of this weight loss [38-39]. Up to 585^{0}C, a 40% weight loss was noted, which could be the result of a metal-oxygen link breaking. It is evident that the bio nanocomposite (TSC/LaCF) was significantly more stable upto 650^{0}C. A slight decrease in weight % between 585 ^{0}C and 650 ^{0}C may be attributed to melting and crystalline range of the nanocomposite (TSC/LaCF).

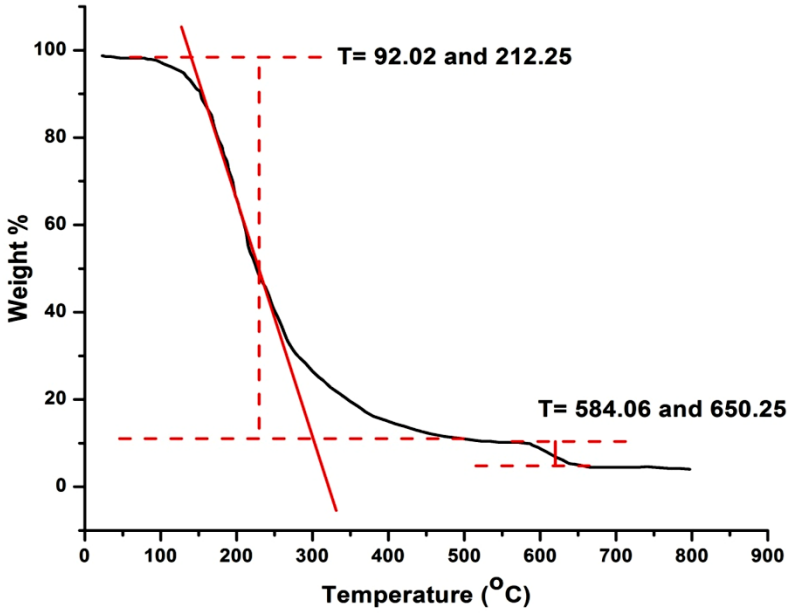

Figure 6: TGA analysis of TSC/LaCF

Effect of experimental conditions on Rhodamine B dye adsorption (Parameter optimization):

Effect of time:

Up to an equilibrium point, which is reached when the removal efficiency continues to rise, the contact duration and dye removal efficiency are directly correlated [40]. By varying the contact period from 20 to 120 minutes and using 50 mg/L of Rhodamine B dye, the range of Rhodamine B dye removal by TSC and TSC/LaCF adsorbents was observed (Figure 7 (a)). The findings show that the elimination of dye molecules increased dramatically up to 80 minutes, after which the removal of Rhodamine B dye particles in both TSC and TSC/LaCF adsorbents gradually stabilized (Figure 7 (a)). To put it another way, before 80 minutes, there will be more active sites for the Rhodamine B dye molecules to attach to the adsorbent surface; after that, the active sites may be filled with Rhodamine B dye molecules [41]. When compared to the adsorption percentage of TSC, the percentage of adsorption in the TSC/LaCF example was shown to be higher.

Effect of adsorbent concentration:

TSC and TSC/LaCF dosages ranged from 50-300 mg/L with all previously specified adsorption parameters held constant, in order to evaluate the impact of adsorbent dosage on Rhodamine B dye removal. As the adsorbent dosage increased, the removal efficiency of Rhodamine B dye improved from 65% to 74% for TSC (Figure 7 (b)) and from 72% to 86% for TSC/LaCF (Figure 7 (b)) [42-43]. The larger surface area and more active sites accessible at higher doses are responsible for this improvement. At dosages of 200 mg/L for TSC and TSC/LaCF, equilibrium was attained. Since the fixed dye concentration did not supply any more Rhodamine B dye molecules to occupy newly added active sites, incremental increases in adsorbent mass beyond these limits did not improve removal efficiency [44]. The main reason TSC/LaCF performs better than TSC is because of its greater surface area.

Effect of pH:

The influence of pH on the adsorption efficiency of Rhodamine B dye using TSC and TSC/LaCF adsorbents was examined by adjusting the solution pH from 2 to 12, while keeping other parameters constant: adsorbent dosage (0.2 g for TSC and 0.1 g for TSC/LaCF), temperature (30°C), shaking time (60 min), and dye concentration (50 mg/L). (Figure 7 (c)) shows the percentage removal of Rhodamine B dye at different pH levels, indicating a clear decline in adsorption efficiency as pH increases from 2 to 6. Maximum removal 70% for TSC and 86% for TSC/LaCF occurred at pH 6, confirming that the adsorption process is favored under acidic conditions [45]. The presence of sulfonic acid groups causes Rhodamine B dye molecules to carry a negative charge in aqueous solutions. Thus, at pH 6, the adsorbent surfaces are positively charged, promoting strong electrostatic attraction between the dye molecules and the adsorbents hence the high adsorption efficiency. Across the pH range of 2–12, the efficiency decreased from 70% to 30% for TSC and from 86% to 40% for TSC/LaCF. This decline is attributed to the electrostatic repulsion that occurs when both the dye molecules and the adsorbent surfaces become negatively charged at higher pH levels [46].

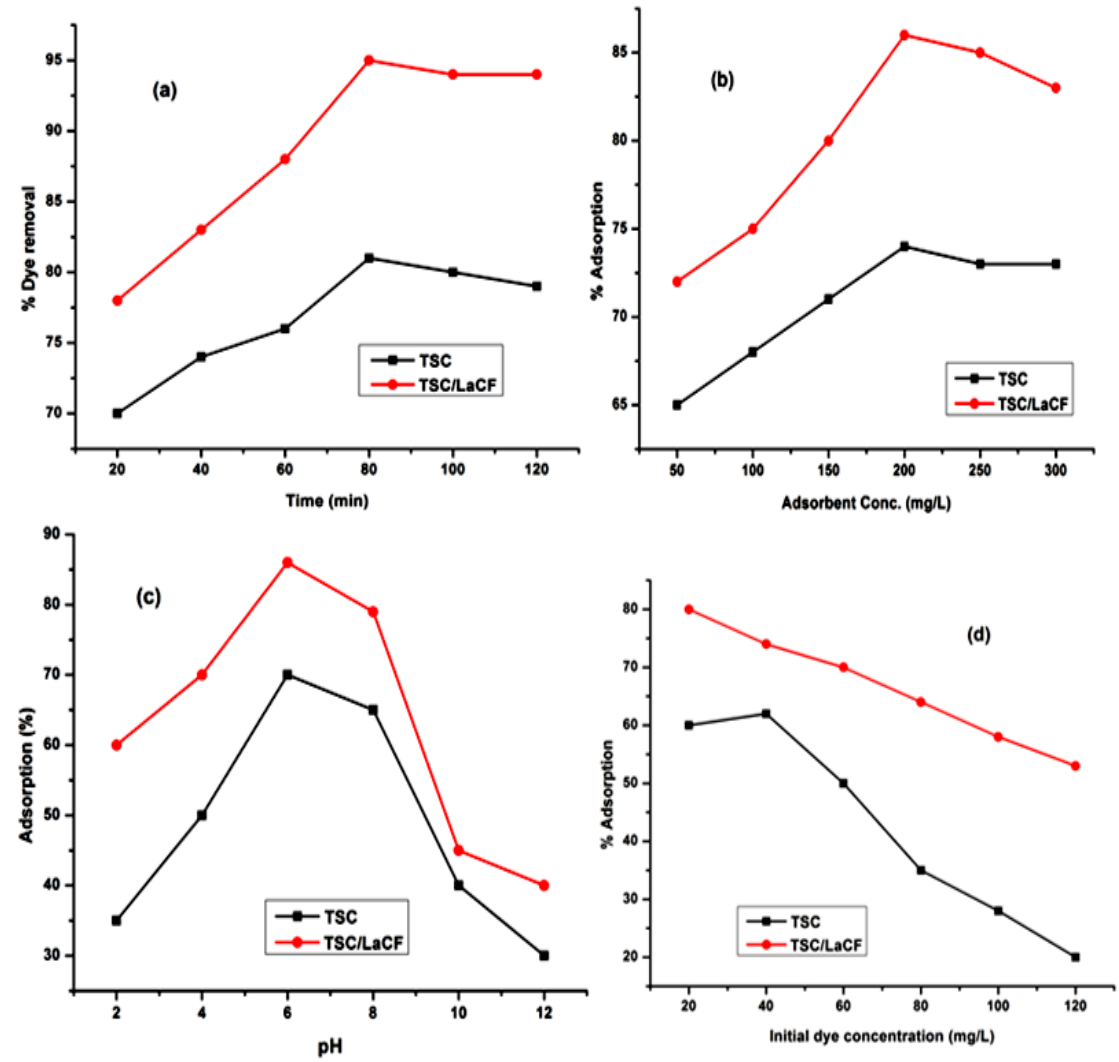

Figure 7: Parameter optimization (a) Effect of time (b) adsorbent concentration (c) pH (d) initial dye concentration on Rhodamine B adsorption

Effect of Dye concentration:

Rhodamine B dye concentrations were varied from 20 to 120 mg/L in order to examine how the initial dye concentration affects adsorption. Other parameters, such as pH 2, contact time, temperature, and adsorbent dosages of 0.2 g TSC and 0.1 g TSC/LaCF, were maintained constant [47]. The removal efficiency of Rhodamine B dye employing TSC and TSC/LaCF adsorbents are shown in (Figure 7 (d)). As can be seen, the adsorption

efficiency gradually declines as the dye concentration increases, falling from 99% to 65% for (TSC/LaCF) and from 98% to 35% for (TSC). This decrease happens as a result of more Rhodamine B dye molecules competing for the few active sites on the adsorbent surface at increasing dye concentrations. Only a certain quantity of dye may be eliminated since the number of active sites stays constant despite variations in starting concentrations [48].

Effect of temperature:

By changing the temperature from 303 K to 333 K while maintaining all other experimental parameters constant, the effect of temperature on the removal of Rhodamine B dye using TSC and TSC/LaCF adsorbents was examined. The proportion of Rhodamine B dye removed at various temperatures is shown in (Figure 8).

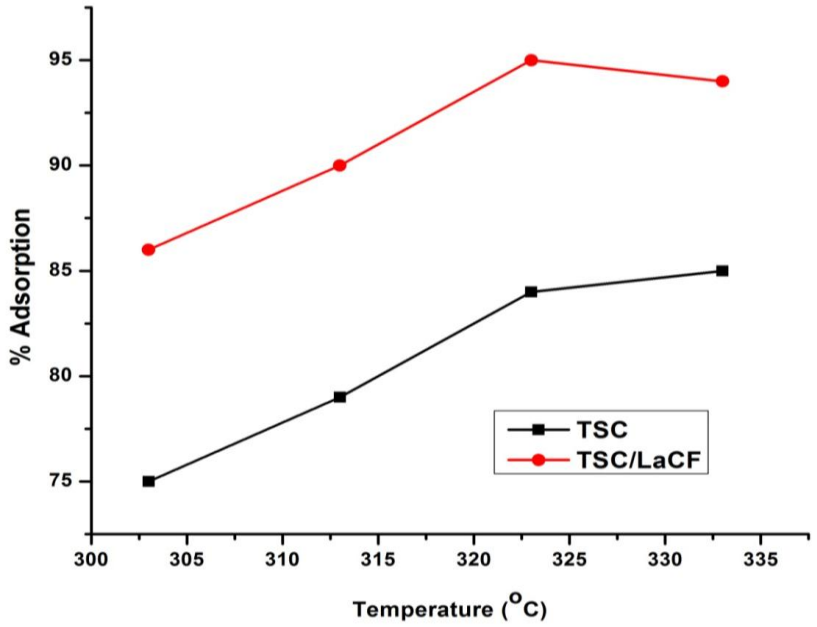

Figure 8: Effect of change in temperature on adsorption of Rhodamine B dye

The findings make it abundantly evident that raising the temperature has a negative impact on the adsorption process. The system's kinetic energy is decreased at lower temperatures, which improve adsorption efficiency. The increased attractive interactions between the deprotonated Rhodamine B dye molecules and the protonated adsorbent surfaces (TSC and TSC/LaCF) are the main cause of this [49–50]. The kinetic energy of the dye molecules grows with temperature, strengthening the electrostatic repulsion between the dye and the adsorbents. Higher temperatures therefore encourage desorption of Rhodamine B dye molecules from the adsorbent surface, which lowers the removal effectiveness.

Thermodynamic studies

The release, retention and mobility of adsorbate molecules on a solid surface at a constant temperature following their introduction into an aqueous medium are generally described by adsorption isotherms. These isotherms offer vital information about the process's overall effectiveness and are crucial for comprehending the mechanisms driving adsorption [51–52]. One of the most used models for assessing surface interactions is the Langmuir adsorption isotherm. It characterizes adsorption as a monolayer process and presupposes a homogeneous surface.

Mathematically, the Langmuir adsorption isotherm model is expressed by (Equation 3):

$$q_e = \frac{q_m K_L C_e}{1+K_L C_e}$$

……..

Equation (3)

The equilibrium concentration, maximum adsorption capacity, and amount of dye adsorbed at equilibrium are denoted by Ce, qm, and qe, respectively, and are represented in mg L^{-1}, mg g^{-1}, and mg g^{-1}. The Langmuir isotherm constant is represented as K_L (L mg^{-1}).

The Freundlich isotherm model, which depicts a multilayer adsorption process, is another variation of the Langmuir adsorption isotherm. It is expressed as follows: (Equation 4):

$q_e = K_F C_e^{1/n}$ …… Equation (4)

The intensity or favorability of the adsorption process is indicated by the Freundlich coefficient n, and the constant $K_{(F)}$ is written as [(mg g^{-1})(L $mg^{-1})^{1.1}$].

According to the Temkin isotherm model, the heat of adsorption decreases linearly as coverage increases due to interactions between the adsorbent and adsorbate. The Temkin isotherm model's mathematical form is shown below (Equation 5 and 6):

$q_e = B\ In\ (A_T\ C_e)$ …… Equation (5)

$B = RT/bT$ ……..... Equation (6)

The heat of adsorption (J/mol), the absolute temperature (K), the Temkin isotherm constant (bT), and the Temkin equilibrium binding constant (L/mg) are represented by the constants B, R, T, and A_T, respectively.

An empirical model that combines elements of the Freundlich and Langmuir isotherms is the three-parameter Redlich-Peterson isotherm [53]. The model is consistent with the Langmuir equation at lower concentrations and the Freundlich isotherm at higher values. Equation 8 provides its mathematical form:

$q_e = \frac{K_R C_e}{1+\alpha_R C_e^{\beta}}$ …….. Equation (7)

The Redlich–Peterson isotherm constants in this model are denoted as K_R (L/g) and α_R (L/mg), and β is a dimensionless exponent related to adsorption intensity that usually ranges from 0 to 1. The adsorption behaviour is shown by the value of β; values less than 1 indicate conformance with the Freundlich model, whereas values greater than 1 indicate the system follows the Langmuir isotherm (Table 1). The isotherm investigations' graphical representations are displayed in Figure 9 (a) and (b).

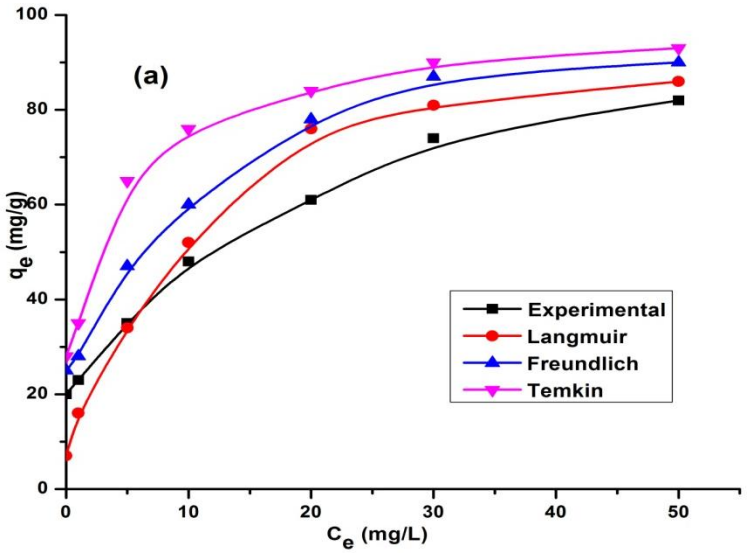

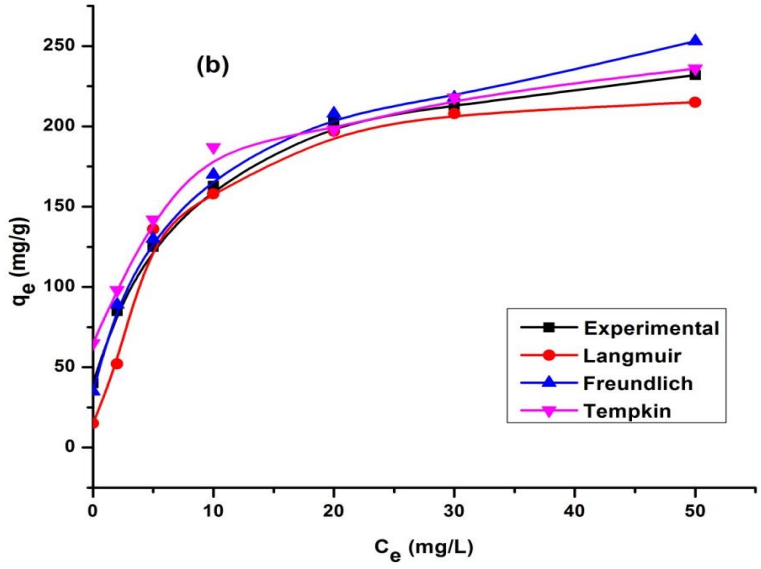

Figure 9: Isotherm assessment of elimination of Rhodamine B dye by (a) TSC and (b) TSC/LaCF

Table 1: Isotherm parameters for Rhodamine B dye removal by TSC and TSC/LaCF.

Sr. No	Adsorbents	TSC	TSC/LaCF
	Parameters	Rhodamine B dye (Adsorbate)	Rhodamine B dye (Adsorbate)
a.	Langmuir		
1.	Q_m (mg/g)	48.25478	98.14782
2.	K_L (L/mg)	0.002	0.04
3.	R_L	0.0189	1.0193
4.	R^2	0.74	0.75
b.	Freundlich		
1.	K_F (L/g)	35.38	45.36
2.	n	2.1	4.2
3.	R^2	0.81	0.83
c.	Tempkin		
1.	K_T (mg/g/h^2)	13.58	38.69
2.	B (g/mg/ h^2)	7.52	19.36
3.	R^2	0.86	0.88

Adsorption Kinetic Study

Kinetic models are essential to an adsorption process because they provide important details on mass-transfer mechanisms, adsorption effectiveness, and the total rate of adsorption. These models explain the rate at which dye molecules are taken up by the adsorbent and then released. Adsorption kinetics generally aid in identifying whether physical or chemical adsorption is occurring. The pseudo-first-order, pseudo-second-order, and Elovich models [54], whose mathematical formulas are shown in (Equation 8-10), are among the kinetic models that are frequently used to evaluate these behaviors.

$q_t = q_e\,(1 - exp(-k_1\,t))$ …… Equation (8)

$q_t = \frac{q_e^2 k_2\, t}{1+q_e k_2\, t}$ …… Equation (9)

$q_t = 1 + \beta_E\, In\,(1 + \alpha_E\, \beta_E\, t$ …….. Equation (10)

Where k_1 and k_2 are the kinetic rate constants (min^{-1}), α is the initial adsorption rate (mg/g.min), β is the Elovich isotherm constant (g/mg), q_e is the amount of adsorbate adsorbed under equilibrium conditions (mg g^{-1}), and qt is the adsorption capacity at a particular time t (mg g^{-1}).

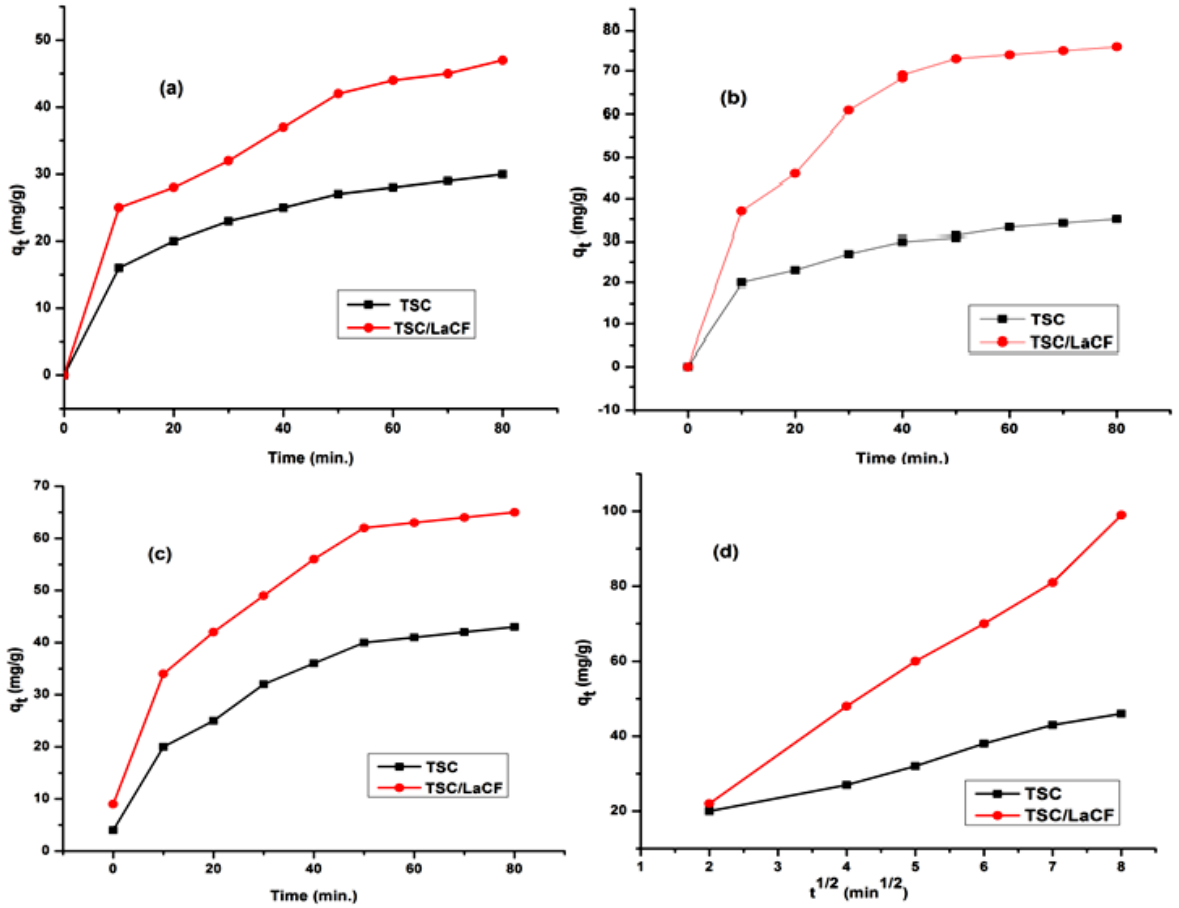

Figure 10: Adsorption Kinetic model assessment (a) pseudo-1st order model, (b) pseudo-2nd order model , (c) Elovich model and (d) diffusion model for TSC and TSC/LaCF.

Table 2: Parameters of Adsorption Kinetic model (a) pseudo-1st order model, (b) pseudo-2nd order model (c) Elovich model and (d) diffusion model for TSC and TSC/LaCF.

Sr. No.	Adsorbents	TSC	TSC/LaCF
	Parameters	Rhodamine B dye (Adsorbate)	Rhodamine B dye (Adsorbate)
a.	Pseudo-1st order		
1.	q_e (mg/g)	14.22	20.36
2.	K_1 (1/h)	0.042	0.058
3.	R^2	98.56	98.85
b.	Pseudo-2nd order		
1.	q_e (mg/g)	16.35	26.74
2.	K_2 (g/mg/min)	0.05	0.06
3.	R^2	98.78	98.94
c.	Elovich		
1.	α(mg/g/h^2)	25.36	51.78
2.	B (g/mg)	0.31	0.37
3.	R^2	99.65	99.78
d.	Diffusion model		
1.	C (mg/g)	11.25	19.72

2.	K_{id}(mg g^{-1} $h^{1/2}$	8.62	8.91
3.	R^2	0.99	0.99

Figure 10 displays the graphical representation of all kinetic models for TSC and TSC/LaCF. All of the models' kinetic parameters are shown in (Table 2). Elovich models, pseudo-1st order models, and pseudo-2nd order models were analysed in order to look at the kinetic parameters. (Table 2) confirms that the Rhodamine B dye adsorption kinetic parameters on TSC and TSC/LaCF nanocomposite have a high regression coefficient of 0.99 [55].

Three stages make up the adsorption process for Rhodamine B dye from a water sample. The first phase, which lasts till 10 minutes, is when the dye's ions move from the aqueous medium to the adsorbate's surface. The intraparticle diffusion of dye to the adsorbate's interior pores can be explained by the second stage, which lasts between 20 and 50 minutes. The third and final step, which lasted up to 80 minutes, detailed how pore diffusion influenced the adsorption process [56]. Therefore, it may be inferred that intraparticle diffusion may be the rate limiting parameter as the curve crosses the origin (Figure 10).

Thermodynamic parameter analysis:
Gibbs free energy (ΔG), enthalpy (ΔH), and entropy (ΔS) were used to assess the system's thermodynamic behaviour. These variables were frequently examined to ascertain whether the adsorption process is feasible, whether it is exothermic or endothermic, and how random or disordered the system is. In this investigation, the concentration of Rhodamine B dye was maintained at 50 mg/L while the temperature was changed from 303 K to 333 K. The adsorbent dosage, contact time, pH, and all other parameters were kept constant. The following equations (11 to 15) were used to compute Gibbs free energy, enthalpy, and entropy.

$K_C = C_{Ae}/C_e$ ………………………………………… (11)

$\Delta G^o = -RTIn\ K_C$ ……………………………………… (12)

$\Delta G^o = \Delta H^o - T\Delta S^o$ ……………………………………… (13)

$In\ K_C = (\Delta H^o/RT)+(\Delta S^o/R)$…………………………… (14)

$log\ K_C = (\Delta H^o/2.303RT)+(\Delta S^o/2.303R)$……………… (15)

The variables C_{Ae}, C_e, T, R, and K_c represent the equilibrium concentration of Rhodamine B dye in the aqueous phase (mg/L), the amount of adsorbate retained on the adsorbent surface (mg/L), the absolute temperature (K), the universal gas constant (8.314 J/mol/K), and the equilibrium constant, respectively.

(Table 3) summarizes the thermodynamic characteristics for the dye Rhodamine B. For TSC and TSC/LaCF, the change in Gibbs free energy (ΔG°) values was negative at all investigated temperatures and continued to rise with temperature, indicating that the adsorption process is both thermodynamically viable and spontaneous (Figure 11). In both situations, the adsorption is exothermic, as indicated by the negative value of enthalpy change (ΔH°) [57–58]. Furthermore, following the adsorption of Rhodamine B dye onto the surface of TSC and TSC/LaCF, the negative entropy change (ΔS°) values (J/mol/K) indicate a decrease in the quantity of randomness at the solid–liquid interface. A comparison between the values of both adsorbate i.e. TSC and TSC/LaCF can be understand easily from (Table 3).

Table 3: Thermodynamic values of adsorption of Rhodamine B dye for TSC and TSC/LaCF

Sr. No.	Temperature	ΔG° (KJ/mol)	
		TSC	TSC/LaCF
1.	300	-6.418	-8.325
2.	313	-6.625	-8.478
3.	323	-6.785	-8.685
4.	333	-6.987	-8.874
5.	ΔH° (KJ/mol)	-8.748	-12.745
6.	ΔS° (J/mol/K)	-30.587	-61.784

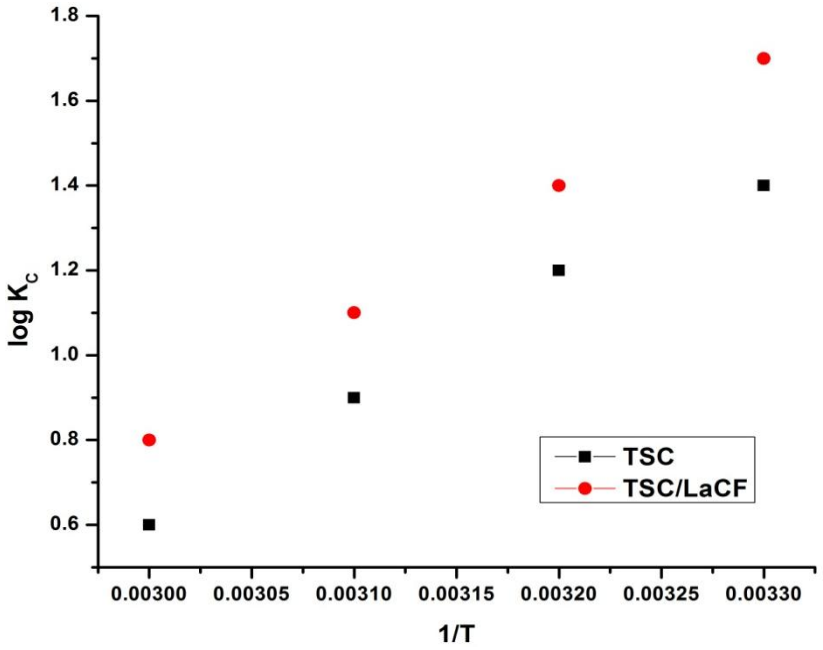

Figure 11: Thermodynamic parameter analysis of adsorption of Rhodamine B dye by TSC and TSC/LaCF

Regeneration study:

Spent adsorbents are often thrown into the environment as garbage, which presents serious disposal issues. These materials can be dangerous and frequently call for expensive, energy-intensive processes like incineration. Environmental dangers are increased by direct dumping. An efficient option is to regenerate used adsorbents, which has benefits including improved material stability and the possibility of recovering valuable adsorbates.

NaOH was deployed as the eluting agent in this investigation to regenerate the exhausted adsorbents. TSC and TSC/LaCF were first saturated with a 50 mg/L Rhodamine B dye solution for a predefined contact period prior to the regeneration process. The dye molecules were desorbable using 0.1 M NaOH after saturation. Desorption is facilitated by the alkalinity of NaOH, which breaks the hydrogen-bonding and electrostatic interactions between the Rhodamine B dye and the surface functional groups of TSC and TSC/LaCF. Before being used again, the adsorbents were cleaned and oven-dried for 120 minutes at 150 °C following desorption.

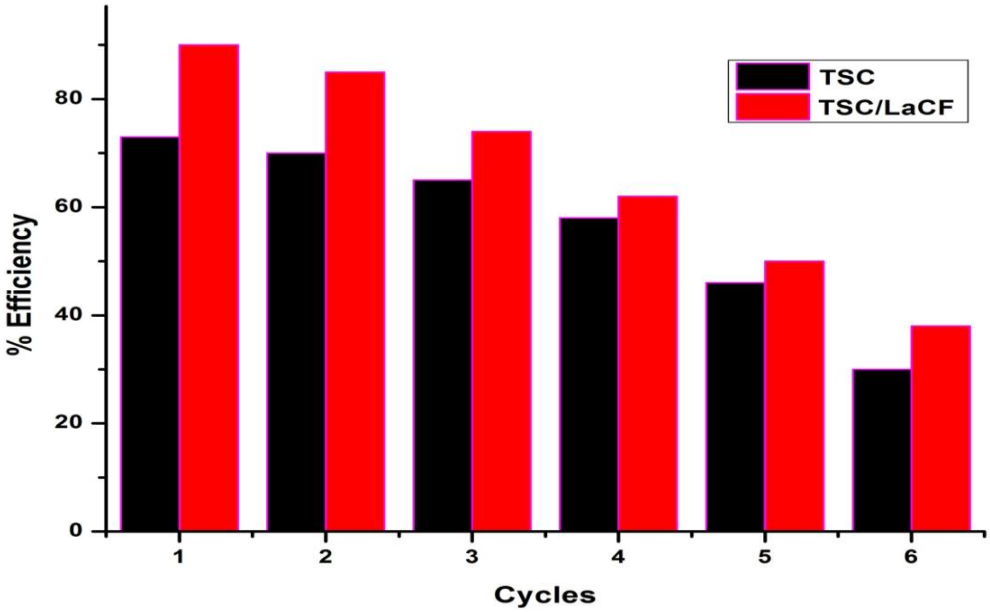

Figure 12: Regeneration of TSC and TSC/LaCF adsorbents

Regeneration efficiencies were from 73% to 30% for TSC and 90% to 38% TSC/LaCF. Both TSC and TSC/LaCF were effectively regenerated for up to six cycles. (Figure 12) depicts the regeneration performance, demonstrating that TSC/LaCF continuously outperformed TSC across all cycles. TSC/LaCF maintained about 50% efficiency after the fifth cycle, while TSC fell to about 46%. The loss of functional groups during repeated regeneration and physical and chemical changes to the adsorbent surface are probably the causes of the slow decline in efficiency [59–60].

IV. CONCLUSION

The modified TSC/LaCF adsorbent derived from stem of *Tinospora cordifolia* was found to be very successful in removing the Rhodamine B dye from the polluted water samples. The analysis of composition, texture and porosity was done by various analytical techniques such as FTIR, BET, VSM, XRD and TGA etc. Adsorption capacity of biochar (TSC) and modified nanocomposite was tested by various thermodynamic and kinetic parameters and results exclaimed the tremendous adsorption capacity of fabricated biochar. The regeneration capacity of the modified biochar was also found to be excellent and tested upto six cycles.

REFERENCES

[1] Lalhriatpuia C, Tiwari D. Biochar-derived nanocomposites for environmental remediation: The insights and future perspectives. Journal of Environmental Chemical Engineering. 2024 Feb 1;12(1):111840.

[2] Cui J, Zhang F, Li H, Cui J, Ren Y, Yu X. Recent progress in biochar-based photocatalysts for wastewater treatment: synthesis, mechanisms, and applications. Applied Sciences. 2020 Feb 4;10(3):1019.

[3] Bartoli M, Giorcelli M, Tagliaferro A. A comprehensive overview on biochar-based materials for catalytic applications. Catalysts. 2023 Sep 30;13(10):1336.

[4] ZHAO D, LI W, JIANG L, SHAN R, CHEN D, YUAN H, CHEN Y. Progress in the Preparation and Performance of Biochar-based Photocatalysts. Ecology and Environment. 2023 Nov 18;32(11):2019.

[5] Yang B, Dai J, Zhao Y, Wu J, Ji C, Zhang Y. Advances in preparation, application in contaminant removal, and environmental risks of biochar-based catalysts: A review. Biochar. 2022 Dec;4(1):51.

[6] Faheem, Du J, Kim SH, Hassan MA, Irshad S, Bao J. Application of biochar in advanced oxidation processes: supportive, adsorptive, and catalytic role. Environmental Science and Pollution Research. 2020 Oct;27(30):37286-312.

[7] Chakhtouna H, Mekhzoum ME, Zari N, Benzeid H, Qaiss AE, Bouhfid R. Biochar-supported materials for wastewater treatment. Applied Water Science Volume 1: Fundamentals and Applications. 2021 May 10:199-225.

[8] Jin M, Zhou Q, Fu L, Wu W. Application of biochar-based catalysts for soil and water pollution control. Topics in Catalysis. 2025 Mar;68(5):591-614.

[9] Visser ED, Seroka NS, Khotseng L. Catalytic properties of biochar as support material potential for direct methanol fuel cell: A review. ACS omega. 2023 Oct 26;8(44):40972-81.

[10] Bhandari G, Gangola S, Dhasmana A, Rajput V, Gupta S, Malik S, Slama P. Nano-biochar: recent progress, challenges, and opportunities for sustainable environmental remediation. Frontiers in Microbiology. 2023 Jul 19;14:1214870.

[11] Zheng Y, Zhou Z, Han F, Fu J, Yu C. Role of Biochar-based Nanocomposites in Soil Remediation: Heavy Metal Immobilization and Ecological Safety. Environmental Chemistry and Safety. 2025 Sep 25;1(2):9600011.

[12] Tibebu S, Worku A, Weldmichael TG. Potential of biochar g-C_3N_4 nanocomposites in soil remediation of 2, 4-D with mechanistic insights and future prospects. Discover Environment. 2025 Dec;3(1):1-8.

[13] Chandrasekaran S, Jadhav S, Selvam SM, Krishnamoorthy N, Balasubramanian P. Biochar-based materials for sustainable energy applications: a comprehensive review. Journal of Environmental Chemical Engineering. 2024 Dec 1;12(6):114553.

[14] Eltaweil AS, Abdelfatah AM, Hosny M, Fawzy M. Novel biogenic synthesis of a Ag@ Biochar nanocomposite as an antimicrobial agent and photocatalyst for methylene blue degradation. ACS omega. 2022 Feb 21;7(9):8046-59.

[15] Amdeha E. Biochar-based nanocomposites for industrial wastewater treatment via adsorption and photocatalytic degradation and the parameters affecting these processes. Biomass Conversion and Biorefinery. 2024 Oct;14(19):23293-318.

[16] Chakhtouna H, Mekhzoum ME, Zari N, Benzeid H, Qaiss AE, Bouhfid R. Biochar-supported materials for wastewater treatment. Applied Water Science Volume 1: Fundamentals and Applications. 2021 May 10:199-225.

[17] Zhang X, Kaštyl J, Casas-Luna M, Havlíček L, Vondra M, Brummer V, Sukačová K, Máša V, Teng SY, Neugebauer P. Microalgae-derived nanoporous biochar for ammonia removal in sustainable wastewater treatment. Journal of Environmental Chemical Engineering. 2022 Dec 1;10(6):108514.

[18] Liu Y, Dai X, Li J, Cheng S, Zhang J, Ma Y. Recent progress in TiO 2–biochar-based photocatalysts for water contaminants treatment: strategies to improve photocatalytic performance. RSC advances. 2024;14(1):478-91.

[19] Eltaweil AS, Abdelfatah AM, Hosny M, Fawzy M. Novel biogenic synthesis of a Ag@ Biochar nanocomposite as an antimicrobial agent and photocatalyst for methylene blue degradation. ACS omega. 2022 Feb 21;7(9):8046-59.

[20] Pathiyar S, Ravi V. Efficient synthesis of carbon nanospheres from waste plastic using a microwave-initiated, biochar-supported bimetallic catalytic method. Fullerenes, Nanotubes and Carbon Nanostructures. 2025 Jul 22:1-3.

[21] Goswami L, Kushwaha A, Singh A, Saha P, Choi Y, Maharana M, Patil SV, Kim BS. Nano-biochar as a sustainable catalyst for anaerobic digestion: a synergetic closed-loop approach. Catalysts. 2022 Feb 1;12(2):186.

[22] Jia Z, Wang H, Yuan S, Zhang W, Zhang D. Green Synthesis of Biochar-Supported Nanoscale Zero-Valent Iron Using Tea Polyphenol for Efficient Cadmium Immobilization in Soil. Nanomaterials. 2025 Sep 23;15(19):1460.

[23] Liu B, Zhang L, Ning K, Yang W. Biochar with nanoparticle incorporation and pore engineering enables enhanced heavy metals removal. Journal of Environmental Chemical Engineering. 2023 Oct 1;11(5):111056.

[24] Zahid M, Khan ZU, Sun J, Muhammad N, Sabahat S, Shah NS, Iqbal J. Biochar-derived photocatalysts for pharmaceutical waste removal, a sustainable approach to water purification. Applied Surface Science Advances. 2025 Mar 1;26:100721.

[25] Nosratabad NA, Yan Q, Cai Z, Wan C. Exploring nanomaterial-modified biochar for environmental remediation applications. Heliyon. 2024 Sep 30;10(18).

[26] Long Z, Wang Z, Huang Q, Jia Y, Jiao Z, Wang Y, Du Y. High-performance adsorption of methylene blue using novel bio-adsorbent based on sargassum fusiforme. Heliyon. 2024 Sep 30;10(18).

[27] Abd El-Monaem EM, Omer AM, El-Subruiti GM, Mohy-Eldin MS, Eltaweil AS. Zero-valent iron supported-lemon derived biochar for ultra-fast adsorption of methylene blue. Biomass Conversion and Biorefinery. 2024 Jan;14(2):1697-709.

[28] Briceño, S.; Reinoso, C. $CoFe_2O_4$-chitosan-graphene nanocomposite for glyphosate removal. *Environ. Res.* 2022, *212*, 113470.

[29] Oliveira, R.V.M.; Santos, A.F.; Santos, M.D.L.; Cunha, G.C.; Romão, L.P.C. Magnetic solid-phase extraction of bisphenol A from water samples using nanostructured material based on graphene with few layers and cobalt ferrite. *Microchem. J.* 2022, *181*, 107741.

[30] Ravichandran D, Megala MA, Anbalagan K, Srivastava P, Al-Dosary MA, Hatamleh AA, Murugesan S. Eco-friendly synthesis of biochar-CoFe2O4 nanocomposites using Ulva lactuca L. for photocatalytic degradation of Congo red and in vitro biological applications. Colloids and Surfaces A: Physicochemical and Engineering Aspects. 2025 May 20;713:136465.

[31] Tharayil JM, Chinnaiyan P, Ramasamy B, Sathasivan A. Biogenic synthesis of Cu/ZnO functionalized biochar nanocomposite: A sustainable approach for visible light-photocatalytic degradation. Environmental Technology & Innovation. 2025 Jun 22:104337.

[32] Zhou Z, Zhao B, Zhang Y, Sun H, Chen J, Huang T. Efficient removal of copper and lead from aqueous solution by magnetic biochar: Magnetization, adsorption, separation, and desorption. Desalination and Water Treatment. 2019 Oct 1;166:24-34.

[33] Takele D, Kalsido AW, Wotee MW. Synthesis of bagasse-derived magnetic biochar for the removal of fluoride from water solution. Water Reuse. 2024 Dec 1;14(4):613-25.

[34] Lin F, Li J, Chen Z, Huang X, Lin W. Fluoride and lead abatement from synthetic and industrial wastewaters using magnetic biochar composite of walnut shell/CuFe2O4/MIL-101 (Al). Journal of Environmental Management. 2025 Sep 1;391:126340.

[35] Mahdavi Z, Peighambardoust SJ, Foroughi M, Foroutan R, Ahmadi M, Ramavandi B. Enhancing fluoride ion removal from aqueous solutions and glass manufacturing wastewater using modified orange peel biochar magnetic composite with MIL-53. Environmental Research. 2024 Dec 1;262:119825.

[36] Brocza FM, Foster SJ, Peacock CL, Jones JM. Synthesis and applications of manganese oxide-biochar composites: A systematic review across catalysis, capacitor and sorption applications. Biomass and Bioenergy. 2024 May 1;184:107201.

[37] Mishra S, Sahoo SS, Debnath AK, Muthe KP, Das N, Parhi P. Cobalt ferrite nanoparticles prepared by microwave hydrothermal synthesis and adsorption efficiency for organic dyes: Isotherms, thermodynamics and kinetic studies. Advanced Powder Technology. 2020 Nov 1;31(11):4552-62.

[38] Khan I, Sadiq S, Wu P, Humayun M, Ullah S, Yaseen W, Khan S, Khan A, Abumousa RA, Bououdina M. Synergizing black gold and light: A comprehensive analysis of biochar-photocatalysis integration for green remediation. Carbon Capture Science & Technology. 2024 Dec 1;13:100315.

[39] El Kawas NM, Zaki AH, Taha M. Methylene blue and methyl orange removal using green rust as a low-cost, sustainable adsorbent and photocatalyst. RSC advances. 2025;15(23):18403-18.

[40] Wang J, Tan Y, Yang H, Zhan L, Sun G, Luo L. On the adsorption characteristics and mechanism of methylene blue by ball mill modified biochar. Scientific Reports. 2023 Dec 1;13(1):21174.

[41] Banerjee S, Chattopadhyaya MC. Adsorption characteristics for the removal of a toxic dye, tartrazine from aqueous solutions by a low cost agricultural by-product. Arabian Journal of Chemistry. 2017 May 1;10:S1629-38.

[42] Marzbali MH, Mir AA, Pazoki M, Pourjamshidian R, Tabeshnia M. Removal of direct yellow 12 from aqueous solution by adsorption onto spirulina algae as a high-efficiency adsorbent. Journal of Environmental Chemical Engineering. 2017 Apr 1;5(2):1946-56.

[43] Andrade CA, Zambrano-Intriago LA, Oliveira NS, Vieira JS, Quiroz-Fernández LS, Rodríguez-Díaz JM. Adsorption behavior and mechanism of oxytetracycline on rice husk ash: kinetics, equilibrium, and thermodynamics of the process. Water, Air, & Soil Pollution. 2020 Mar;231(3):103.

[44] Lin D, Wu F, Hu Y, Zhang T, Liu C, Hu Q, Hu Y, Xue Z, Han H, Ko TH. Adsorption of dye by waste black tea powder: parameters, kinetic, equilibrium, and thermodynamic studies. Journal of Chemistry. 2020;2020(1):5431046.

[45] Wang S, Zhao H, Liu J, Wang X, Li J, Shi E, Wang C, Yang J, Zhang Z. A study on and adsorption mechanism of ammonium nitrogen by modified corn straw biochar. Royal Society Open Science. 2023 Feb 8;10(2):221535.

[46] Darabdhara J, Ahmaruzzaman M. Recent developments in MOF and MOF based composite as potential adsorbents for removal of aqueous environmental contaminants. Chemosphere. 2022 Oct 1;304:135261.

[47] Singh S, Prajapati AK, Chakraborty JP, Mondal MK. Adsorption potential of biochar obtained from pyrolysis of raw and torrefied Acacia nilotica towards removal of methylene blue dye from synthetic wastewater. Biomass Conversion and Biorefinery. 2023 May;13(7):6083-104.

[48] El Maguana Y, Elhadiri N, Benchanaa M, Chikri R. Activated carbon for dyes removal: modeling and understanding the adsorption process. Journal of Chemistry. 2020;2020(1):2096834.

[49] Wang J, Tan Y, Yang H, Zhan L, Sun G, Luo L. On the adsorption characteristics and mechanism of methylene blue by ball mill modified biochar. Scientific Reports. 2023 Dec 1;13(1):21174.

[50] Hameed BH, Mahmoud DK, Ahmad AL. Equilibrium modeling and kinetic studies on the adsorption of basic dye by a low-cost adsorbent: Coconut (Cocos nucifera) bunch waste. Journal of hazardous materials. 2008 Oct 1;158(1):65-72.

[51] Ambaye TG, Vaccari M, van Hullebusch ED, Amrane A, Rtimi SJ. Mechanisms and adsorption capacities of biochar for the removal of organic and inorganic pollutants from industrial wastewater. International Journal of Environmental Science and Technology. 2021 Oct;18(10):3273-94.

[52] Liu Z, Zhang FS. Removal of lead from water using biochars prepared from hydrothermal liquefaction of biomass. Journal of hazardous materials. 2009 Aug 15;167(1-3):933-9.

[53] Liu QY, Yang F, Sun XF, Liu ZH, Li G. Preparation of biochar catalyst with saccharide and lignocellulose residues of corncob degradation for corncob hydrolysis into furfural. Journal of material cycles and waste management. 2017 Jan;19(1):134-43.

[54] Lu K, Yang X, Gielen G, Bolan N, Ok YS, Niazi NK, Xu S, Yuan G, Chen X, Zhang X, Liu D. Effect of bamboo and rice straw biochars on the mobility and redistribution of heavy metals (Cd, Cu, Pb and Zn) in contaminated soil. Journal of environmental management. 2017 Jan 15;186:285-92.

[55] Islam IU, Ahmad M, Ahmad M, Rukh S, Ullah I. Kinetic studies and adsorptive removal of chromium Cr (VI) from contaminated water using green adsorbent prepared from agricultural waste, rice straw. Eur. J. Chem. 2022 Mar 31;13:78-90.

[56] Hu X, Ding Z, Zimmerman AR, Wang S, Gao B. Batch and column sorption of arsenic onto iron-impregnated biochar synthesized through hydrolysis. Water research. 2015 Jan 1;68:206-16.

[57] Hikmat K, Aziz H, Fatah NM. Advancements in Application of Modified Biochar as a Green and Low-cost Adsorbent for Wastewater Remediation From Organic Dyes.

[58] Goswami L, Kushwaha A, Kafle SR, Kim BS. Surface modification of biochar for dye removal from wastewater. Catalysts. 2022 Jul 26;12(8):817.

[59] Trivedi Y, Sharma M, Mishra RK, Sharma A, Joshi J, Gupta AB, Achintya B, Shah K, Vuppaladadiyamd AK. Biochar potential for pollutant removal during wastewater treatment: A comprehensive review of separation mechanisms, technological integration, and process analysis. Desalination. 2025 Jan 2:118509.

[60] Verma N, Devi NL. Removal of atmospheric pollutants using biochar: preparation, application, regeneration and its future research. Air Quality, Atmosphere & Health. 2025 Apr;18(4):1205-24.